Flutter Analysis of a Morphing Wing Technology Demonstrator: Numerical Simulation and Wind Tunnel Testing[a]

Andreea KOREANSCHI[1], Mehdi ben HENIA[1], Olivier GUILLEMETTE[1], Francois MICHAUD[1], Yvan TONDJI[1], Oliviu SUGAR GABOR[1], Ruxandra Mihaela BOTEZ*[,1], Manuel FLORES SALINAS[1]

*Corresponding author
[1]LARCASE Laboratory of Applied Research in Active Control, Avionics and Aeroservoelasticity, École de Technologie Supérieure
Montreal, H3C1K3, Quebec, Canada
koreanschiandreea@yahoo.com, benheniamehdi@hotmail.com, oliviu.guillemette@gmail.com, francaos7@hotmail.com, yvanschool@yahoo.fr, oliviu_sugar@yahoo.com, Ruxandra.Botez@etsmtl.ca*
manuel.flores-salinas.1@ens.etsmtl.ca

DOI: 10.13111/2066-8201.2016.8.1.10

Received: 05 January 2016 / Accepted: 27 January 2016
Copyright©2016. Published by INCAS. This is an open access article under the CC BY-NC-ND license (http://creativecommons.org/licenses/by-nc-nd/4.0/)

Abstract: *As part of a morphing wing technology project, the flutter analysis of two finite element models and the experimental results of a morphing wing demonstrator equipped with aileron are presented. The finite element models are representing a wing section situated at the tip of the wing; the first model corresponds to a traditional aluminium upper surface skin of constant thickness and the second model corresponds to a composite optimized upper surface skin for morphing capabilities. The two models were analyzed for flutter occurrence and effects on the aeroelastic behaviour of the wing were studied by replacing the aluminium upper surface skin of the wing with a specially developed composite version. The morphing wing model with composite upper surface was manufactured and fitted with three accelerometers to record the amplitudes and frequencies during tests at the subsonic wind tunnel facility at the National Research Council. The results presented showed that no aeroelastic phenomenon occurred at the speeds, angles of attack and aileron deflections studied in the wind tunnel and confirmed the prediction of the flutter analysis on the frequencies and modal displacements.*

Key Words: *morphing wing, aeroelasticity, flutter analysis, control, wind tunnel experiment*

I. INTRODUCTION

Today's aircrafts are not just flying machines; their design relies on a compromise between aerodynamic efficiency, structural optimization, fuel consumption minimization and environment requirements. This compromise asked for new methods in flight management,

[a] *The paper surpasses the page limit imposed by the journal due to the presentation of a high number of both numerical and experimental results. These results were needed to offer a better understanding of the research conducted on the Morphing Wing Tip demonstrator, particularly the research done on aeroelastic behaviour.*

in aircraft design, structure, aerodynamics and controls. Many types of answers were found depending on the objective problem; for the minimization of fuel consumption or for the improvement of the aircraft flight envelope, the morphing methods are considered the most promising solutions. Morphing consists in changing the structure or appearance of an aircraft during flight by modifying the wing sweep[1], span[2], chord[3] or camber[4, 5], by the high lift devices[6, 7] or the fuselage, for small aircraft and for UAV's[8, 9]. A state of the art in aircraft morphing, particularly on wing morphing, were given by Sofla et al[10], Vasista S, Tony L., Wong K.[11] and Barbarino et al[12]. The common features of all morphing configurations are a flexible structure, or skin. and free or unconventional structural elements, e.g. actuators or morphing mechanisms. These configurations need aero-elastic studies[13] to prove that they meet safety requirements demanded in aircraft industry and therefore flutter or divergence phenomena would not occur at certain flight conditions (speeds, angles of attack or aileron deflection angles). For example, many of the morphing structures use composite materials, for example Huo S, Yuan Z, Wang F and Yue Z[14] have studied the aero-elastic effects of composite wings using Nastran-Fluent coupling with implications for engineering applications. Many other aero-elastic studies were performed to prove the excellent qualities of the morphing structures with regards to their static and dynamic aero-elastic effects. Pecora R, Magnifico M, Amoroso F and Monaco E. have proposed the study of wing twist morphing on the aircraft roll control[15] and also they explored the flutter effects of a morphing wing trailing edge[16]. Xie C, Liu Y and Yang C[17] have explored methods to realize aero-elastic static and flutter analysis using lifting –line theory for very flexible wings, which were encountered at high-altitude long-endurance aircrafts with high-aspect-ration wings. Also, Murua J, Palocios R and Peiro J[18] investigated the effects of chord-wise flexibility on the dynamic stability of compliant airfoils using a classical two-dimensional aero-elastic model expanded with an additional degree of freedom to capture time-varying camber deformations. A review of the progress made in aerodynamic and aero-elastic analysis of flapping wings was presented by Shyy W, Aono H and Chimakurthi S.K.[19]. In 2002, the Aerospace Industry Association of Canada, the Government of Quebec and key university research centers formed the Consortium for Research and Innovation in Aerospace Quebec (CRIAQ) to encourage mostly Civil Aviation research. One of their projects, called CRIAQ 7.1, was focused on shape changing wings and was realized between teams from Canadian aerospace industry companies, such as Bombardier and Thales, the IAR-NRC Research Center and two universities, the École de Téchnologie Supérieure and École Polytechnique[20-22]. The purpose of the CRIAQ 7.1 project was to prove that controlling the position of the transition point and pushing it towards the trailing edge using shape-changing techniques can reduce the drag coefficient, and implicitly, the fuel consumption[23-25]. As shown in the obtained results, it was possible to obtain up to 40% laminar flow improvement on a laminar airfoil-based wing model, and at the same time to achieve up to 20% drag coefficient reduction by using active control with smart material alloy actuators (SMA). A subsequent aeroelastic study proved that the morphing technique would not induce flutter phenomena during wind tunnel testing[26-27]. In addition, many breakthroughs were achieved in active open-loop and closed-loop control using Proportional – Integrate (PI)[28-29] and Fuzzy Logic based controllers in wind tunnel testing[30-32]under the auspices of this same project. The research presented in this paper was completed in the frame of the CRIAQ MDO 505 project realized as an international collaboration between Canadian and Italian industries, universities and research centers. The purpose of this project was to demonstrate the structural, aerodynamic and control abilities of a real aircraft wing tip equipped with an adaptive upper surface and an adaptive aileron during subsonic wind tunnel tests. The

novelty of the project consists in the design, analysis and manufacturing of an aerodynamically and structurally optimized real wing tip. The wing tip was tested for structural 1g loads, and, during these tests, the composite upper surface and the adaptive aileron were controlled with electrical actuators situated in the wing and in the aileron boxes. The present paper is concerned with the aero-elastic behavior, specifically flutter phenomenon, of the wing tip during wind tunnel testing, especially at the Mach number of 0.25 which was the highest speed to be tested in the wind tunnel. The behavior of the wing was of outmost concern due to the composite flexible skin attached on all four sides of the wing box and of the electrical actuation system installed inside. For this purpose, a comparison of the flutter behavior was made between the wing model with flexible composite upper surface and its version with classic aluminium upper surface. To these configurations, a rigid aileron was added, actuated by an external actuator rigidly fixed to the wing mounting support under the wind tunnel floor. Finally, acceleration results obtained over a range of 1 second from the accelerometers installed on the wing were presented to show that the wing demonstrator suffered no aero-elastic phenomena during wind tunnel tests.

II. PRESENTATION OF THE RESEARCH CONTEXT

The research presented in this present paper was done within the framework of the international CRIAQ MDO505 Morphing Wing project. The participants in this project were the Ecole de Technologie Supérieure (ETS), Ecole Polytehnique of Montreal and University of Naples 'Federico II' as academia research partners, the Canadian National Research Council (CNRC) and the Italian Aerospace Research Center (CIRA) as research center partners, and Bombardier Aerospace, Thales Canada and Alenia Aermacchi as industrial partners. The objectives of the project were to design, manufacture and control a wing demonstrator based on a real aircraft wing tip equipped with both a conventional and an adaptive aileron. The CRIAQ MDO 505 project was a continuation of the earlier research project CRIAQ 7.1, and was aimed at a higher Technical Readiness Level (TRL) by considering a real wing internal structure, a certifiable electric control system and controllers. The objectives of the active morphing wing tip project were mainly: (1) an improvement of the aerodynamic performance of the wing, through the active control of the boundary layer transition from laminar to turbulent states, (2) the design and manufacturing of a morphing wing model that withstand gust loads of up to 1g, and (3) the design, implementation and integration of control systems and a morphing mechanism to control the shape of the wing in wind tunnel experiments. The morphing wing demonstrator represents a wing section situated between the fuel tank section and the winglet. Figure 1 presents the position of the wing section under discussion.

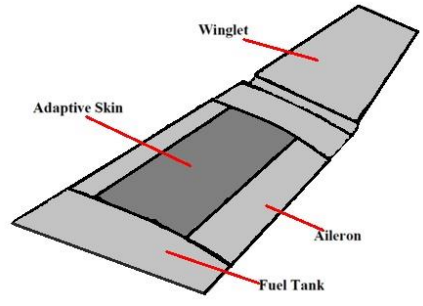

Figure 1. Layout and position of the morphing skin on the aircraft wing

Unlike a full wing, the demonstrator does not display a sweep angle, this aspect being eliminated to reduce the tridimensional effects of the flow on the wing. In addition, at this section of the wing the aileron would occupy half of the wing section's span, but for the demonstrator, the span of the aileron was chosen to equal that of the wing.

The wing demonstrator internal structure contains the same components as a real wing: ribs, spars, stiffeners, etc, which was designed in accordance with the designs and positions of such structural elements on a real wing. Figure 2 shows the structural elements of the CRIAQ MDO 505 project morphing wing concept, where the morphing skin is not shown.

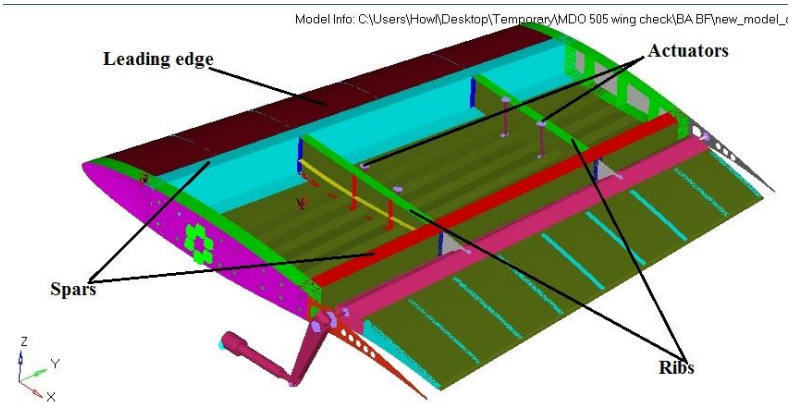

Figure 2. Structural elements of the CRIAQ MDO 505 morphing wing concept

However, the leading edge was simplified by using a thin aluminium skin supported by ribs. The dimensions of the wing demonstrator were slightly adapted to respect the dimensions of the IAR-NRC subsonic wind tunnel chamber which has a section of 2m x 3m. Therefore, the wing demonstrator has a span of 1.5 m and a root chord of 1.5 m. Despite the modifications that were made to the structure of the demonstrator, its trapezoidal shape was conserved (tapered wing), with a taper angle of 8° on both leading and trailing edge sides. The chord varies progressively between 1.5m at its root to 1.08m at its tip and has a maximum thickness of 143 mm at the root section. Figure 3 presents the geometrical design of the wing demonstrator and its main dimensions.

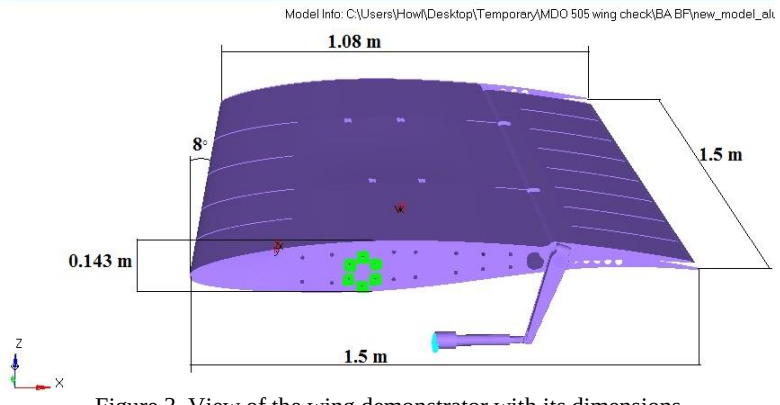

Figure 3. View of the wing demonstrator with its dimensions

The aileron's hinge was located at 72% of the chord. Two types of ailerons were designed and manufactured. One aileron was structurally rigid, while the other was a new morphing aileron. Both ailerons were designed to be attached to the same hinge axis on the wing box, and both were able to undergo a controlled deflection between -7° and +7°.

In order to ensure the best multidisciplinary optimization of the wing-tip, structural constraints were, in a first step, discussed and imposed. The multidisciplinary optimization was a combination of integrated aerodynamic, structural and control optimization processes. The aerodynamic optimization was carried at airfoil level, and was done by controlling four points situated on the upper surface of the airfoil. These four points corresponded to the leading and trailing edge fixation points of the skin defining the morphing region, and to two vertically mobile points, situated at 32% and 48% of the chord, which represent the actuator's displacements. The four points were used in conjunction with cubic splines method[33] to retrace the upper surface of the airfoil and obtain a new shape. For a specific combination of angles of attack, speeds and aileron deflection angle, the mobile points were displaced with values between -3.5 mm and 3.5 mm during the optimization iteration process until it was achieved the objective of delaying the transition from laminar to turbulent flow. Further information on the aerodynamic optimization process and its results, obtained both numerically and experimentally, was presented by Koreanschi et al[34-36] and Sugar et al[37].

In order to maintain the structural integrity of the demonstrator, the aerodynamic optimization was constraint by geometry and skin deformation limitations. The positions of the leading and trailing edge spars represented the main geometric constraint. They were situated at 20% and 65% of the chord, and these positions represent the actual delimitation of the morphing skin. In return, to better comply with the aerodynamic spline reconstruction, the skin was fixed to the spar caps, and it remained continuously tangent to them at all moments.

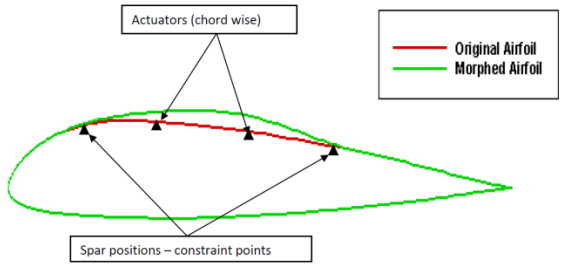

Figure 4. Example of the morphed versus original airfoil shape with spar optimization constraint.

Another structural constraint for the aerodynamic optimization was the imposition of a maximum allowable skin length deformation. Such a constraint was imposed because without it the skin would have been submitted to high elastic deformations which would have affected the quality and quantity of structural optimization process needed for the composite skin. The maximum allowable deformation was set at +/- 0.03% of the original spline length which was equivalent to the chord-wise skin length. Further details on the structural optimization of the wing and on the composite skin optimization process can be found in Michaud, F.[38]

III. DETAILED FINITE ELEMENT MODEL PRESENTATION

The model used for the flutter analysis was a Detailed Finite Element Model or DFEM. The morphing wing demonstrator was constituted of several structural elements: two spars, four ribs, 12 stiffeners (six for each surface), six leading edge ribs, nine trailing edge ribs, five skins (two skins for the wing box, one for the leading edge and two for the trailing edge), four internal actuators and one external aileron actuator. The finite element model or FEM was designed using Altair Hypermesh software[39]. Two FEM models were created, one model

was equipped with a traditional aluminium upper surface skin of 3mm constant thickness, and another model with carbon fiber composite upper surface optimized for morphing behavior, this latter model corresponded to the wing demonstrator that was tested in the wind tunnel. The purpose of this research was to determine whether the replacement of the aluminium skin with constant thickness by a composite skin with variable number of plies and thickness per ply would affect the dynamic aero-elastic behavior of the wing demonstrator.

The FEM model has used of a mixture of 3D, 2D and 1D elements, where the 1D elements were used to represent the connectors, the aileron shaft and the four internal actuators. The 1D elements used for connectors to model the connections between the skins, spars and ribs were of the type SPRING, and were associated to PBUSH properties which defined the material and type of connections used. The four internal actuators were modeled using BEAM elements; Figure 5 presents an example of the modeled actuators installed inside the wing box. A BEAM element is a 1D representation of a simple beam with its associated physical and geometrical properties. This type of element is capable of sustaining all efforts in translation and rotation at its extremities. The cross-section for this type of element was defined by the menu Hyperbeam where the dimensions are defined by the user. For the four actuators, the diameter of the BEAM was chosen to be 25 mm which was representative of the real actuator diameter, while the material associated with the actuators was aluminium. RBE2 rigid elements were added to the extremes of the BEAM to ensure a representative contact surface with the upper and lower skins. The RBE2 defines a rigid body whose independent degree of freedom was specified at a single ‘master’ node, while the dependent degrees of freedom were specified at a number of ‘slave’ nodes chosen by the user. The aileron shaft was also modeled using BEAM elements of circular area with a variable diameter along the span – the diameter of the shaft varies between 25 mm at the root to 12.5 mm at the tip of the wing – and steel material properties were assigned to it.

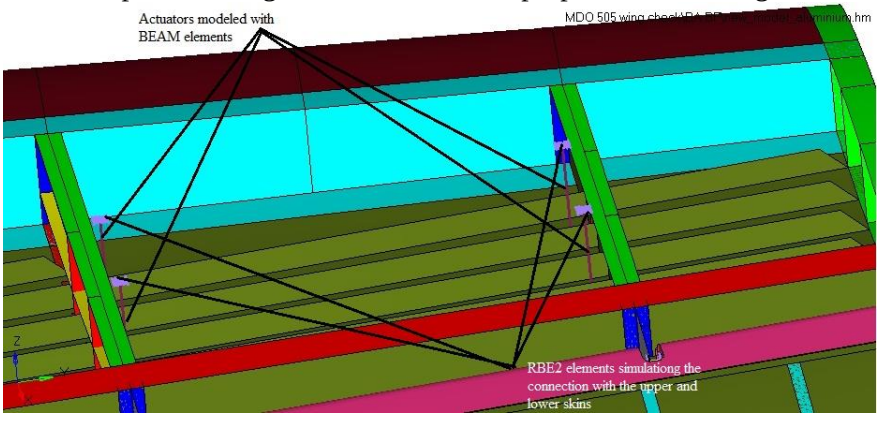

Figure 5. View of the BEAM elements modeling the actuators and their connections to flexible skin

The rigid fixation of the wing demonstrator to a steel mount, as it was installed in the wind tunnel, was done using rigid elements called RBE3, Figure 6 shows a representation of the rigid fixation and constrains applied. The RBE3 elements define a rigid body similar to the RBE2 element described in the previous paragraph with the difference that the RBE3 element allows the natural deformation of the rigidly fixed structure which minimizes the stress concentration that usually were associated with RBE2 elements. The RBE3 were constrained in all directions and similar constraints were used for the area surrounding the mounting holes.

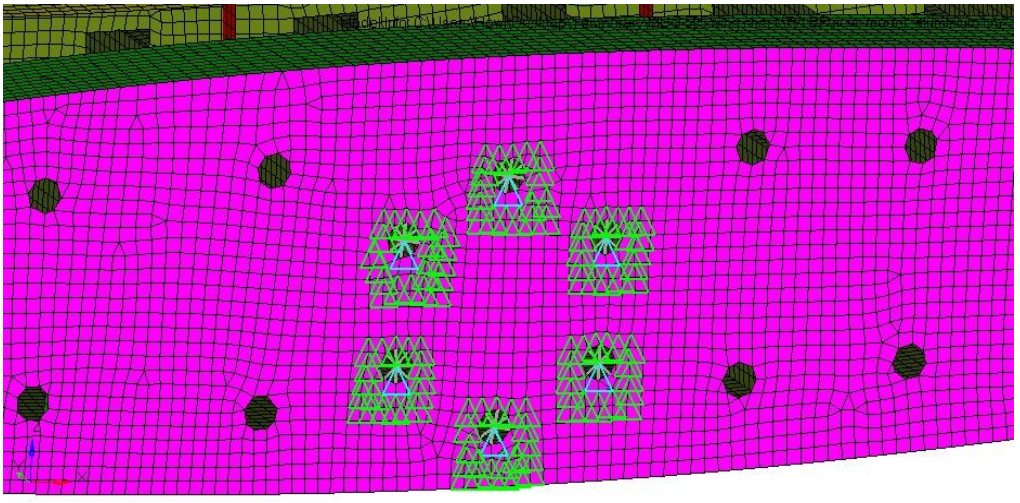

Figure 6. RBE3 rigid elements and constraints simulating the mounting of the wing in the subsonic wind tunnel

All structural components of the wing, with the exception of the aileron leading edge, aileron shaft and external actuator were defined as surfaces and were meshed using a combination of quadrilateral CQUAD4 and triangular CTRIA3 elements in order to ensure the optimal progression of the mesh on the trapezoidal shape of the wing. All surface elements were of the type SHELL to which either PSHEL or PCOMP properties were assigned in function of the section of the wing.

The PSHELL or PCOMP properties ensured a thickness and a material was associated to each element. The PCOMP property characterized the composite skin section of the wing and it allowed the user to indicate the number of plies and the direction of the carbon composite fibers in both chord- and span-wise directions, as well as the thickness for each individual ply.

The PCOMP property was given to all elements that meshed the upper surface skin and stringers of the wing demonstrator. All other surfaces of the wing, that were not composite, were assigned PSHELL property with aluminium as associated material (E = 71GPa, G = 27GPa and ν = 0.33).

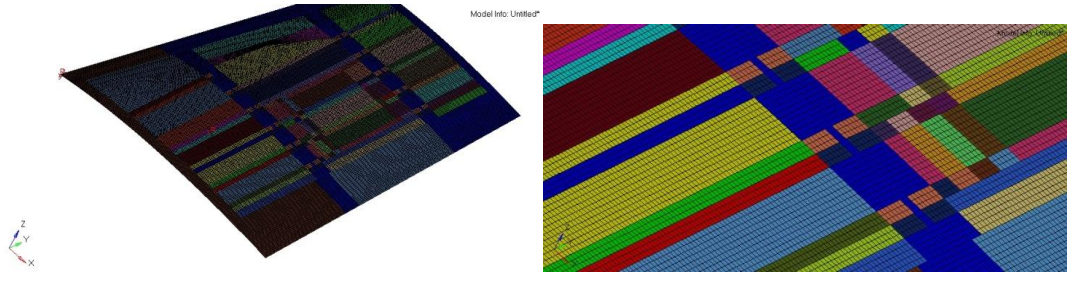

Figure 7a. Left – View of the upper surface skin designed in composite material; Right – Close-up view of the upper-surface skin

The different colors, shown in Figure 7a, represent various sections of the upper surface skin that have different number of plies, different thickness per ply and different orientations of the carbon fibers.

For wing model with the aluminium upper surface skin, the same number and type of elements was used as for the composite skin.

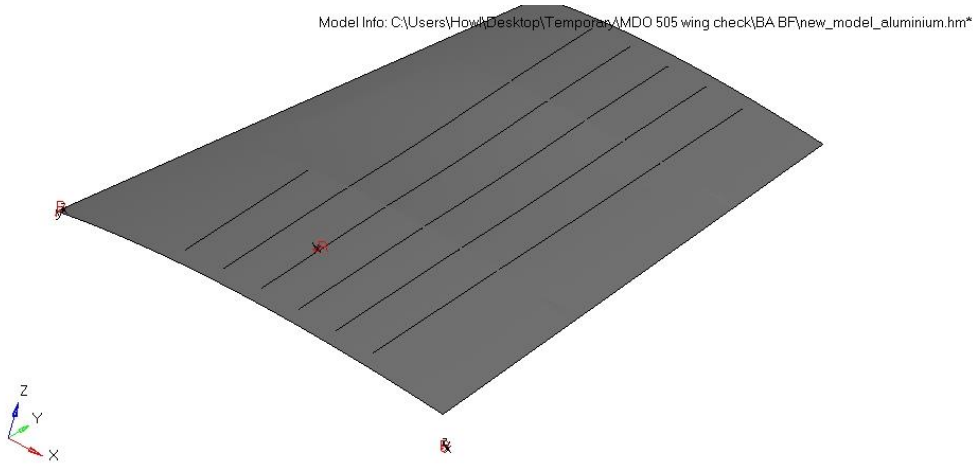

Figure 7b. View of the upper surface skin of the wing in aluminium

The aileron's external actuator was meshed using 3D tetrahedral elements of the CTETRA type to which PSOLID and steel properties were associated. The PSOLID properties associate a number and a reference system for each CTETREA element. The aileron leading edge was also meshed using CTETRA elements but the material associated to it was aluminium.

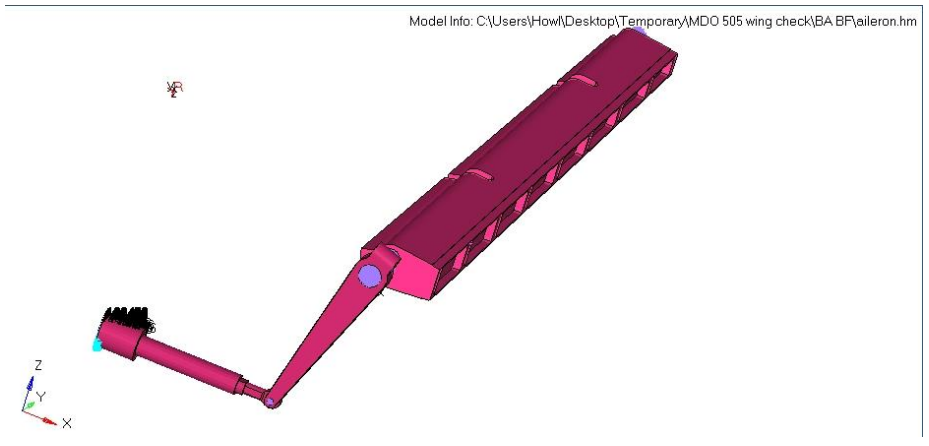

Figure 8. View of the aileron leading edge, shaft and actuator

IV FLUTTER ANALYSIS

The FEM models used during the flutter analysis were described in section III above. The Hyperworks software Hypermesh was used for the development of the FEM model and to export all information as a Nastran deck file,'.bdf', for MSC Patran/Nastran[40] aero-elastic flutter analysis. MSC Patran was used to correct errors that were obtained from importing a model from a platform to another, from Hypermesh to Patran in this case. Most of the errors encountered concerned nodes duplication, errors in the definition of the boundary conditions, and different definitions for the multi- point constraint (MPC) – the multi-point constraint have a different name associated in each of the software used.

Figure 9 presents the workflow diagram for the aero-elastic analysis of the wing demonstrator.

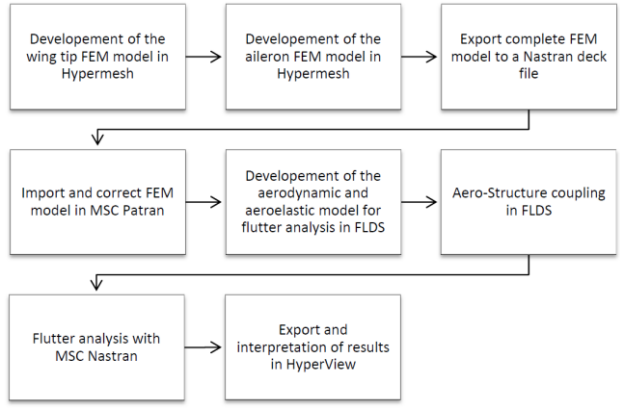

Figure 9. Workflow diagram of the aeroelastic flutter analysis of the CRIAQ MDO wing tip

1. Aero – Structure modeling

For the flutter analysis a definition of the aerodynamic model and its coupling with the structural FEM model was needed, and MSC's Flight and Loads Dynamics (FLDS) software was used to create them. The aerodynamic model was defined through reference lifting surfaces or flat plates. For the FEM wing model, two lifting surfaces were created: one for the wing box and another for the aileron. The reference lifting surfaces were defined by a reference chord (mean aerodynamic chord), span and sweep angle (for the model presented in this paper no sweep angle was considered). To minimize the time needed for doing mesh convergence, MSC Nastran recommendations[41] were used to establish the number of aerodynamic elements or DLM boxes needed to obtain the best results:

$$\frac{DLM_boxes}{\frac{v}{fc}} > 15 \tag{1}$$

where v is the reference speed, f is the reduced frequency of the flow and c is the reference chord of the wing. In this case, eight boxes in the span directions with 5 boxes in the chord direction, for a total of 40 DLM boxes, were used to model the wing body lifting surface, and eight boxes in span direction with three boxes in chord direction were used to model the aileron lifting surface. Figure 10 presents the wing tip demonstrator FEM model with lifting surfaces for the wing body and aileron.

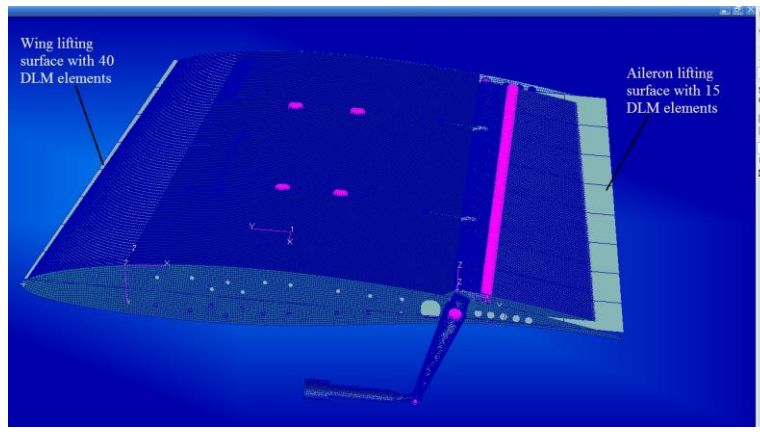

Figure 10. View of the model with lifting surfaces

The flow properties are described by the Mach - reduced frequencies (Mk), the velocity and densities list. All three are requirements of the PK method used for the flutter analysis.

The coupling of the structural and aerodynamic models was realized through splining or interpolation between the structural and aerodynamic grids. The Thin Plate Spline (TPS) method that was provided by the FLDS software was used. The 'Thin Plate Spline' is an interpolation method used for structures which have elements in the three-dimensional space (x, y, z), and it was developed from the Infinite Plate Spline (IPS) method which is used for structures developed in a bi-dimensional space (2D plates) [42]. Due to lack of information for the treatment of the selection of the structure nodes or their location for the splining process, 'two test procedures' were proposed to find the optimal combination of the number and positions of nodes. The first test proposes a selection of all the nodes on the upper and lower surfaces. The test showed that such a high number of nodes made the analysis almost impossible in terms of calculation time; thus, some of the resulted files – e.g. the '.DBALL' file hosting the splining matrix or the '.F06' file hosting the analysis results - attained prohibitive dimensions – several Gb of data which were difficult to manage. In the second test, several combinations of number of nodes and locations were used. Six groups were created, each group contained 137, 194, 266, 298, 330 and 391 nodes, respectively. The results of the second test made for finding the optimal number and positions of nodes are presented in Figures 11 and 12 for the first two modes in terms of frequency versus speed curves. It can be observed that regardless of the number of points (N) used or their location on the upper and lower surfaces, the results are close and the differences are negligible; still, a sufficient number of nodes, no less than the number of DLM boxes, and an even distribution of the nodes were desired.

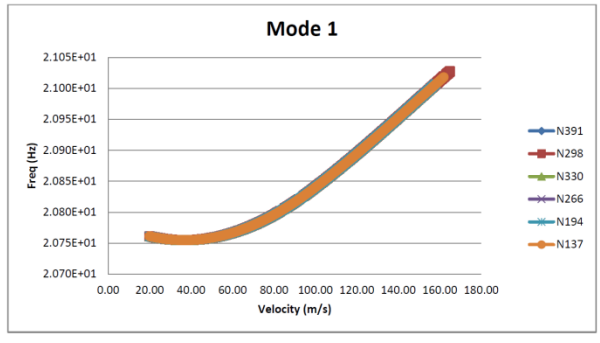

Figure 11. Frequency versus velocities for 1st Mode obtained by using six combinations of number of nodes

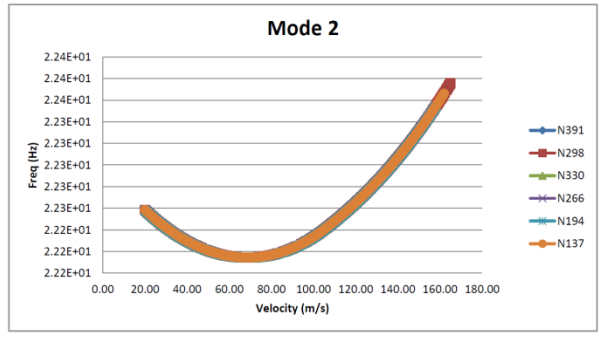

Figure 12. Frequency versus velocities for 2nd Mode obtained by using six combinations of number of nodes

For the finite element model of the wing equipped with flexible upper surface and an aileron, a number N of 110 nodes was used for the splining process.

2. P-K method

As mentioned before, the aeroelastic flutter analysis was done using the PK method offered by Nastran. This method was chosen due to its pertinence in the results it offers, especially at low speeds regimes, in which the presented test speeds were also considered[43, 44].
The fundamental equation describing the PK method is given by equation (2):

$$\left[\frac{V^2}{L^2}Mp^2 + K - \frac{1}{2}\rho V^2 Q(ik)\right]\{q\} = 0. \tag{2}$$

For simplification purposes, equation (2) excludes the structural damping matrix C. *M* and *K* represent the mass and stiffness matrixes, *V* is the speed and *Q(ik)* the vector of external forces. In equation (2), *p* is the Laplace non-dimensional parameter that is defined by equation 3:

$$p = g + ik \tag{3}$$

$$g = \gamma k \tag{4}$$

where, *g* represents the damping coefficient, calculated using the reduced frequency *k* and an under-relaxation coefficient *γ*, as shown in equation (4).

Rodden[45] has modified the *PK* equation by adding an aerodynamic damping matrix to it, thus in Nastran solver the *PK* equation is expressed as shown in equation (5):

$$\left[\frac{V^2}{L^2}Mp^2 + k - \frac{1}{2}\rho V^2 \frac{Q^I}{k}p - \frac{1}{2}\rho V^2 \frac{Q^R}{k}\right]\{q\} = 0. \tag{5}$$

Where Q^I and Q^R are the imaginary and real parts of the force matrix *Q*(ik). Equation (5) can also be expressed in the following state space formulation:

$$[A - pI]\{q\} = 0. \tag{6}$$

where *p* represents the spectre of all the eigenvalues. Its solution is expressed by the eigenvalues of matrix A:

$$A = \begin{bmatrix} 0 & 1 \\ -M^{-1}\left[k - \frac{1}{2}\rho V^2 \frac{Q^R}{K}\right] & -M^{-1}\left[-\frac{1}{2}\rho V^2 \frac{Q^I}{K}\right] \end{bmatrix} \tag{7}$$

where *A* and *q*, from equation (7), include the speeds and modal displacements. For this nonlinear system, the solution is found through an iterative process.

3. Flutter analysis results

As mention in the above section III, two FEM models were created; the first model had a traditional aluminium upper surface while the second model had an optimized flexible composite upper surface skin. The purpose of the analysis was to demonstrate that although the wing model with composite skin was designed and optimized for its morphing behavior, its aero-elastic behavior remained close to that of the wing normally equipped with an aluminium skin of constant thickness. Also, the analysis served to demonstrate that for the speeds used during the wind tunnel tests, no flutter phenomenon was expected to occur. The maximum speed at which the wing demonstrator was tested in the wind tunnel was 85 m/s or Mach number of 0.25.

Table 1 present the first five natural modes obtained for the wing models, as the natural frequencies of the structure were calculated first during the flutter analysis.

Table 1. Comparison between the natural frequencies of the wing models with upper surface aluminium skin and composite skin

Mode No.	Frequency(Hz)	
	Wing Model with aluminium upper surface skin	Wing Model with composite upper surface skin
I	2.04E+01	2.08E+01
II	2.17E+01	2.22E+01
III	7.31E+01	7.37E+01
IV	1.28E+02	1.29E+02
V	1.38E+02	1.39E+02

From the table above, it can be summarized that there is almost no change in the values of the natural frequencies whether the upper surface of the wing demonstrator was made from aluminium and had a constant thickness or from optimized carbon composite material with variable thickness.

Table 2 presents the frequencies and damping values for the first 5 modes for the following three speeds used during wind tunnel tests: 50 m/s, 70 m/s and 90 m/s.

Table 2. Comparison of the frequencies and damping values for speeds of 50, 70 and 90 m/s

Mode No.	Speed (m/s)	Wing Model with Aluminium upper surface		Wing Model with Composite upper surface	
		Frequency (Hz)	Damping	Frequency(Hz)	Damping
I	50	2.04E+01	-5.82E-03	2.08E+01	-4.02E-03
	70	2.04E+01	-8.26E-03	2.08E+01	-5.70E-03
	90	2.04E+01	-1.05E-02	2.08E+01	-7.23E-03
II	50	2.16E+01	-5.62E-03	2.21E+01	-7.23E-03
	70	2.16E+01	-7.84E-03	2.21E+01	-1.01E-02
	90	2.16E+01	-1.02E-02	2.21E+01	-1.32E-02
III	50	7.29E+01	-8.26E-03	7.35E+01	-8.12E-03
	70	7.29E+01	-1.32E-02	7.35E+01	-1.31E-02
	90	7.29E+01	-1.82E-02	7.35E+01	-1.81E-02
IV	50	1.28E+02	1.40E-04	1.29E+02	-6.27E-04
	70	1.28E+02	-7.90E-04	1.29E+02	-1.55E-03
	90	1.28E+02	-1.72E-03	1.29E+02	-2.48E-03
V	50	1.38E+02	-8.07E-03	1.39E+02	-7.02E-03
	70	1.38E+02	-9.29E-03	1.39E+02	-8.20E-03
	90	1.38E+02	-1.05E-02	1.39E+02	-9.36E-03

From Table 2 it can be observed that no flutter tendencies appear at any of the studied speeds. The analysis was performed up to a speed of 110 m/s which is the maximum speed of the IAR-NRC wind tunnel, and no flutter behavior was predicted. In Figures 13 and 14, the evolution of the frequency and damping with speed is presented for the five modes mentioned above.

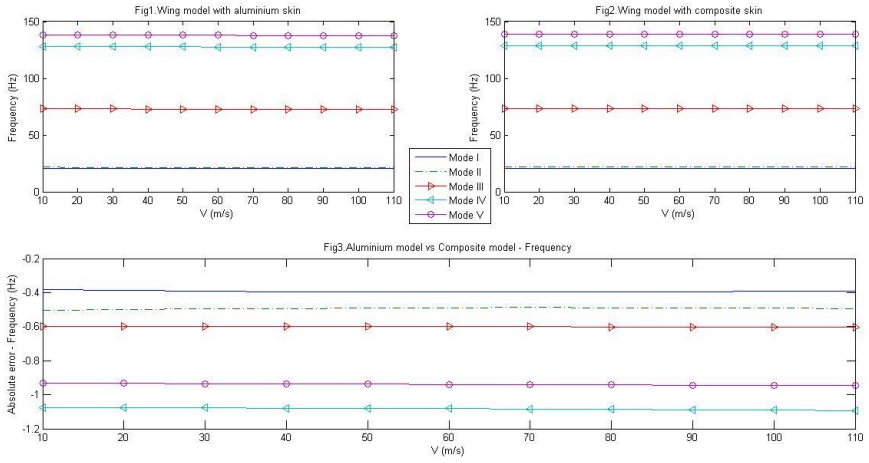

Figure 13. Frequencies of the first five modes over a range of speeds

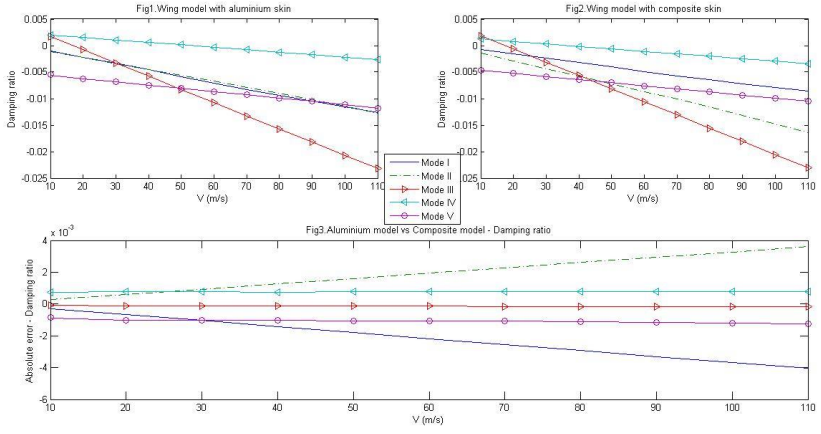

Figure 14. Damping behaviour of the first five modes over a range of speeds

From Figure 13 it is observable that the wing model with composite upper surface skin has close frequency to those obtained for the wing model equipped with aluminium upper surface skin, the average absolute error was less than 1Hz. From Figure 14, it can be deduced that for the first and second mode the composite skin has some influence in the damping behavior of the model. For mode I, the vibrations of the wing model with composite skin are dampened slower than for the wing model with aluminium skin. For mode II, the vibrations of the wing model with composite skin are dampened faster than for the wing model with aluminium skin.

Also, from Figure 14.1 and 14.2, for the wing with composite skin, the first and second modes show a tendency to separate, whereas for the model with aluminium skin the two modes almost overlap. The behavior of the wing models for the last three modes is almost the same, the absolute error being approximately +/- $0.5*10^{-3}$.

Figures 15 to 18 present, in terms of modal displacements, the behaviour of each mode for both aluminium and composite upper surface wing models, with the first and second modes representing the bending behavior around the x, respectively the y axis; the third mode representing the torsion behavior while the 4th mode representing the coupling behavior between torsion and bending.

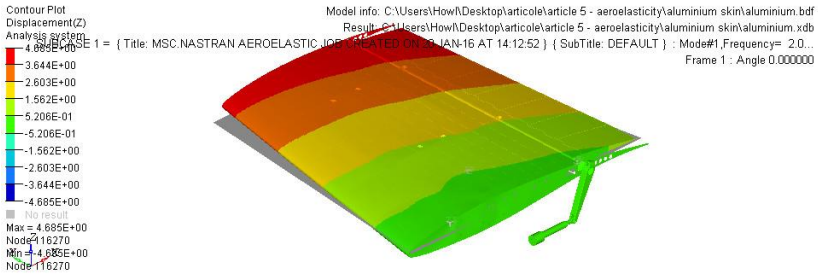

15 a)

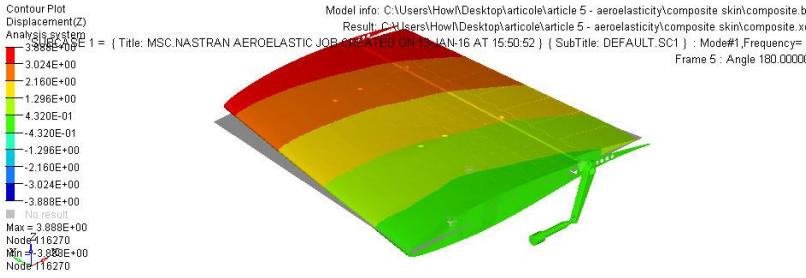

15 b)

Figure 15. First mode behavior – bending

Figure 15 a) presents the first mode behavior for the FEM model with upper surface aluminium skin, while Figure 15 b) presents the first mode for the FEM model with upper surface composite skin. The behavior is identical for both models but the displacement of the composite skin model is smaller than for the aluminium skin model, which shows that the model with composite skin was developed, through the optimization process, to be more rigid in the span direction.

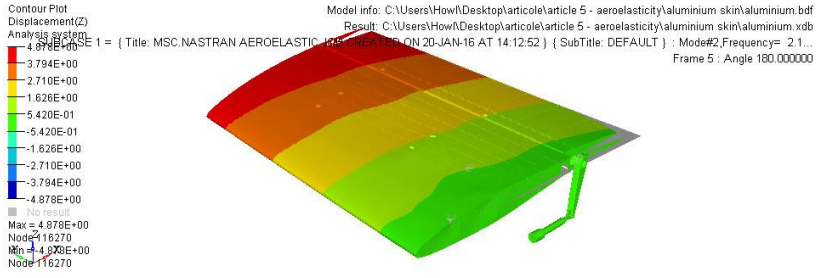

16 a)

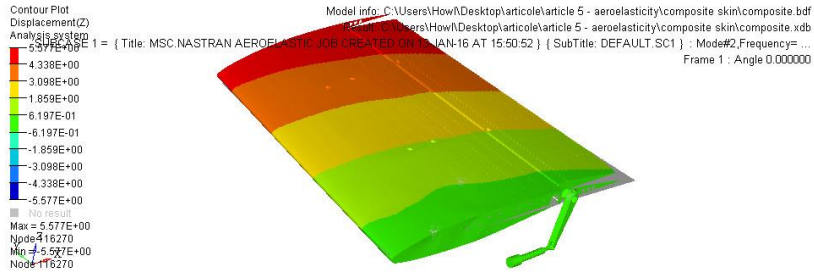

16 b)

Figure 16. Second mode behaviour – lateral bending

Figure 16 a) presents the second mode behavior for the FEM model with upper surface aluminium skin, while Figure 16 b) presents the second mode for the FEM model with upper

surface composite skin. The behavior is identical for both models but the displacement of the composite skin model is higher than for the aluminium skin model because the model with composite skin was developed to be more flexible in the chord wise direction.

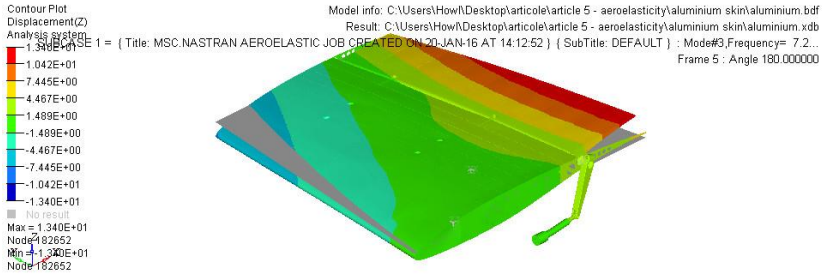

17 a)

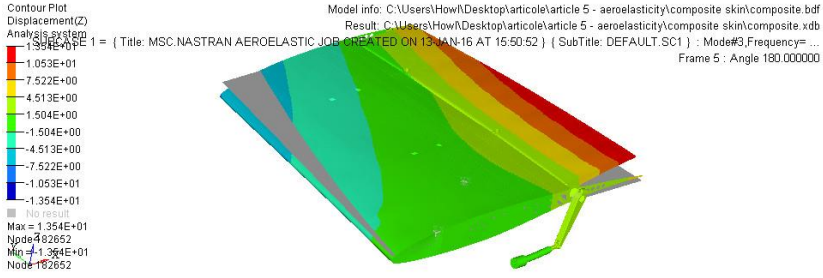

17 b)

Figure 17. Third mode behaviour – torsion

Figure 17 a) presents the third mode behavior for the FEM model with upper surface aluminium skin, while Figure 17 b) presents the third mode for the FEM model with upper surface composite skin. The behavior is torsion for both models, where the maximum and minimum displacements are almost identical. For this mode, the type of material and optimization of the upper surface skin seems to have no effect on the behavior of the models.

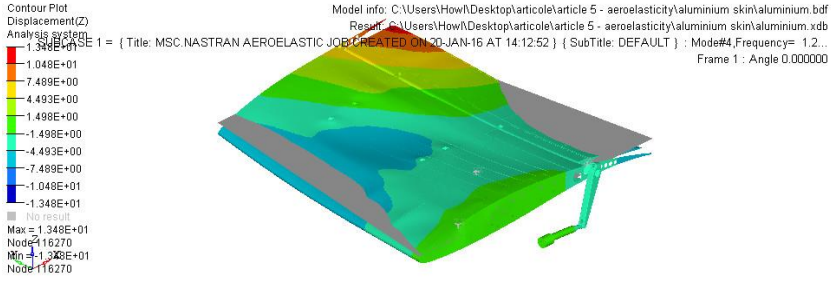

18 a)

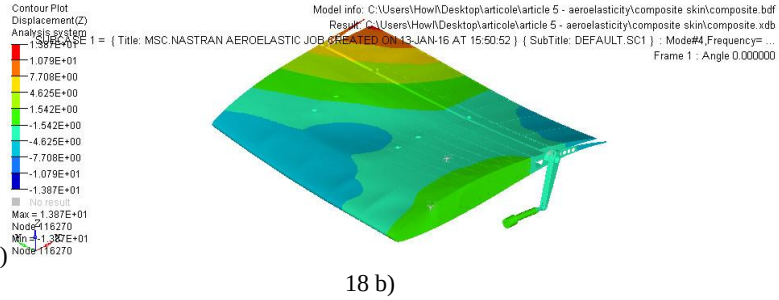

18 a)

18 b)

Figure 18. Fourth mode – Coupling between torsion and bending

Figure 18 a) presents the fourth mode behavior for the FEM model with upper surface aluminium skin, while Figure 18 b) presents the fourth mode for the FEM model with upper surface composite skin. The difference in the overall maximum displacement between the two FEM models is negligible, but the behavior of the aluminium upper surface skin model close to the leading edge is slightly different than the behavior of the composite skin model, which has a smaller displacement deformation in that area.

This difference is due to the bending component of the mode; in the fourth mode the bending deformation takes place in the span direction, and as shown in Figure 15, the composite upper surface wing model is more rigid in the span direction due to the constraint that the composite skin had to be capable of supporting the same type of loads as the aluminium upper surface skin would.

Based on the aero-elastic results presented above, the optimization process of the upper surface skin which includes the introduction of variable thickness in both span and chord directions as well, and different material, has succeeded in obtaining a skin that has the same overall behavior as a traditional aluminium skin, but, is more rigid span-wise to account for the constraint of being capable of resisting to the same loads as the aluminium skin and more flexible chord-wise to permit deformation using two actuation points in the chord direction. The analysis has also shown that there was no possibility of flutter phenomena occurring for the speeds at which the wing demonstrator was tested and even for speeds beyond the capacity of the wind tunnel, which has shown that the model was structurally rigid for the tests that took place.

V. WIND TUNNEL TESTING

In this section the testing of the wing demonstrator and the results obtained from the accelerometers installed inside the wing are presented.

1. Wind tunnel description

The wind tunnel tests were performed at the 2 m x 3 m atmospheric closed circuit subsonic wind tunnel of the National Research Council Canada. This atmospheric wind tunnel can operate at a maximum Mach number of 0.33.

The upper surface flexible skin of the wing demonstrator was equipped with 32 high precision Kulite piezoelectric-type transducers[46] for pressure measurement on the flexible skin and the data was processed to determine the laminar-to-turbulent transition location. These sensors were installed in two staggered lines (with 16 Kulite sensors on each line), situated respectively at 0.600 m and 0.625 m from the wing root section. In addition to the Kulite piezoelectric sensors, at the same two span-wise stations, 60 static pressure taps were installed (30 taps on each line), on the wing leading edge, lower surface and aileron, thus providing complete experimental pressure distribution around the wing cross section at 40% of the wing span. The pressure sensors were installed in a staggered fashion to minimize the interference between them.

The experimental measurements also included the use of a wake rake pressure acquisition system, to measure the wing profile drag at different span-wise positions, and to use a wind tunnel balance for measuring the aerodynamic forces and moments

Figure 19 presents the MDO 505 CRIAQ project morphing wing model installed in the tunnel test section, viewed from both the leading edge (Figure 19 a) and the trailing edge (Figure 19 b).

(a) (b)

Figure 19. MDO 505 wing model setup in the wind tunnel test section; (a) front view, (b) rear view

To avoid the possibility of damaging the wing tip model during wind tunnel testing, and to be able to observe the first installments of the flutter vibrations, if such a case occurred despite the flutter analysis results, three accelerometers were installed on the wing. The accelerometer model used was the ADXL326[47], which is a small, low power, complete 3-axis accelerometer with signal conditioned voltage outputs. The ADXL 328 card is an analog three axes accelerometer of $\pm 16g$ of full scale range, with a zero g voltage of $1.5\ V$ and an output sensitivity of $57\ mV/g$ when it is powered at $3\ Vs$. It contains a poly-silicon surface micro-machined sensor and signal conditioning circuitry for the implementation of open-loop acceleration measurement architecture. The output signals are analog voltages that are proportional to the measured acceleration. The accelerometer can measure the static acceleration of gravity in tilt sensing applications, as well as dynamic acceleration, resulting from motion, shock, or vibration. For the present case, the measurements were performed for wing vibration and motions resulted from the wind tunnel testing at various speeds.

The three accelerometers were installed in the wing box, aileron and wind tunnel balance respectively as shown in Figure 20.

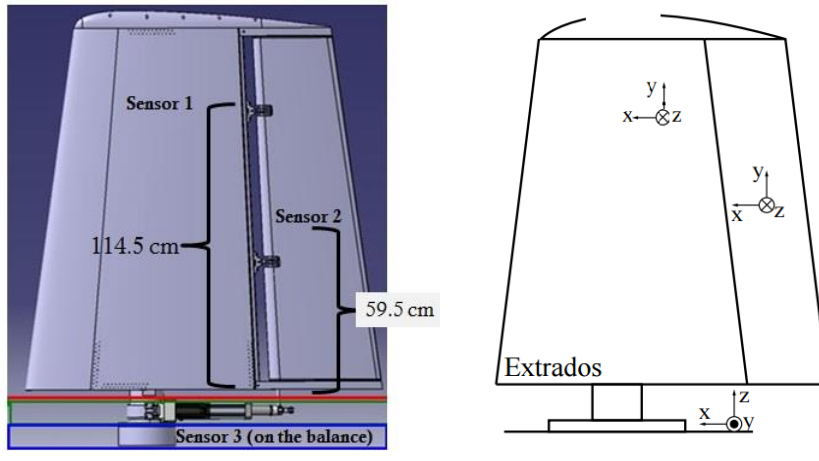

Figure 20. Positions and orientations of the accelerometers on the wing

2. Accelerometers results

The data recorded by the accelerometers is presented for several cases that were studied in the wind tunnel tests. The cases, for which graphical results are presented, are shown in Table 3.

Table 3. Wind tunnel test cases for which accelerometer results are presented

Case number	Speed (m/s)	Angle of attack (°)	Aileron deflection angle (°)
1	50	-3	-2
2	50	-1.4	4
3	85	-1.5	-4
4	85	-2	5
5	85	-3	1

To quantify the magnitude of the vibration of the wing and aileron, it is necessary to find to boundaries of the amplitude of the recorded acceleration points. Therefore, we suppose that the recorded waveform is the sum of sinusoids representing the vibration modes acceleration as shown in equation (8).

$$A(t) = \sum_i A_{X_i} \sin\left(2\pi f_{X_i} t + \phi_{X_i}\right) \vec{\imath} + \sum_i A_{Y_i} \sin\left(2\pi f_{Y_i} t + \phi_{Y_i}\right) \vec{\jmath} + \sum_i A_{z_i} \sin\left(2\pi f_{z_i} t + \phi_{z_i}\right) \vec{k} \tag{8}$$

where $A_{X_i}, A_{Y_i}, A_{Z_i}$ represent the acceleration amplitudes of the torsional mode on the *X* axis, lateral-bending mode on the *Y*-axis, and the bending mode on the *Z*-axis, respectively, and where $f_{X_i}, f_{Y_i}, f_{Z_i}$ are the frequencies, and $\phi_{X_i}, \phi_{Y_i}, \phi_{Z_i}$ are the phases.

The demonstration of the boundary is next shown only for the acceleration on the *Z*-axis, but is the same for the accelerations on the *X* and *Y* axes. By considering two sinusoids (vibration modes), so that the bending acceleration equals to the sum of that two sinusoids, we can write:

$$A_Z(t) = A_{z_1} \sin\left(2\pi f_{z_1} t + \phi_{z_1}\right) + A_{z_2} \sin\left(2\pi f_{z_2} t + \phi_{z_2}\right) \tag{9}$$

The associated root mean square value verifies equation (10):

$$\left(RMS_{Z_1+Z_2}\right)^2 = RMS_{Z_1}^2 + RMS_{Z_2}^2 \tag{10}$$

where

- $RMS_{Z_1+Z_2}$ is the root mean square of A_Z
- RMS_{Z_1} is the root mean square of the first sinusoid, and $RMS_{Z_1} = \frac{A_{z_1}}{\sqrt{2}}$
- RMS_{Z_2} is the root mean square of the second sinusoid, and $RMS_{Z_2} = \frac{A_{z_2}}{\sqrt{2}}$

Equation (10) gives

$$\left(RMS_{Z_1+Z_2}\right)^2 = \frac{A_{Z_1}^2 + A_{Z_2}^2}{2} \tag{11}$$

$$\Rightarrow \quad 4\left(RMS_{Z_1+Z_2}\right)^2 = 2\left(A_{Z_1}^2 + A_{Z_2}^2\right) \tag{12}$$

It can be shown that $2\left(A_{Z_1}^2 + A_{Z_2}^2\right) \geq \left(A_{Z_1} + A_{Z_2}\right)^2$ for all $A_{Z_1} \epsilon$ R and $A_{Z_1} \epsilon$ R

$$\begin{cases} \left(A_{Z_1} - A_{Z_2}\right)^2 \geq 0 \\ => \ A_{Z_1}^2 + A_{Z_2}^2 \geq 2A_{Z_1}A_{Z_2} \\ => \ 2\left(A_{Z_1}^2 + A_{Z_2}^2\right) \geq 2A_{Z_1}A_{Z_2} + A_{Z_1}^2 + A_{Z_2}^2 \\ => 2\left(A_{Z_1}^2 + A_{Z_2}^2\right) \geq \left(A_{Z_1} + A_{Z_2}\right)^2 \end{cases} \tag{13}$$

It is evident that equation (12) leads to

$$4\left(RMS_{Z_1+Z_2}\right)^2 \geq \left(A_{Z_1} + A_{Z_2}\right)^2 \tag{14}$$

$$=> 2 * RMS_{Z_1+Z_2} \geq A_{Z_1} + A_{Z_2} \geq \left|A_{Z_1}\sin\left(2\pi f_{Z_1}t + \phi_{Z_1}\right) + A_{Z_2}\sin\left(2\pi f_{Z_2}t + \phi_{Z_2}\right)\right| \tag{15}$$

$$=> \quad \left|A_{Z_1}\sin\left(2\pi f_{Z_1}t + \phi_{Z_1}\right) + A_{Z_2}\sin\left(2\pi f_{Z_2}t + \phi_{Z_2}\right)\right| \leq 2 * RMS_{Z_1+Z_2} \tag{16}$$

Equation (16) has been demonstrated for two sinusoids, but this inequality can be extended for *n* sinusoids, with *n* ϵ N. It can be rewritten under the following form:

$$\left|\sum_{i=1}^{n} A_{Z_i}\sin\left(2\pi f_{Z_i}t + \phi_{Z_i}\right)\right| \leq 2 * RMS_{Z_1+\cdots+Z_n} \tag{17}$$

Table 4 gives the boundaries of the recorded accelerations on the three axes X, Y and Z.

Table 4. Limits or boundaries of the recorded accelerations

Case number	X_max_aileron (g)	Y_max_aileron (g)	Z_max_aileron (g)	X_max_ wing (g)	Y_max_ wing (g)	Z_max_ wing (g)
1	0.1201	0.1153	0.1659	0.0937	0.0924	0.0956
2	0.1086	0.1182	0.1913	0.0754	0.0777	0.0845
3	0.1283	0.1403	0.4247	0.0836	0.0994	0.1188
4	0.0864	0.1070	0.4287	0.0492	0.0709	0.1120
5	0.0990	0.1164	0.4533	0.0583	0.0860	0.1052

In Figures 21 to 25 (a) and (b), the post processed data from the accelerometers was presented as behavior of the acceleration (measured in *g*) with time for a time range of 1s and their correspondent power spectra density. The accelerations in time domain are presented only for the bending vibration (Z-axis) because it's much greater that the other axis.

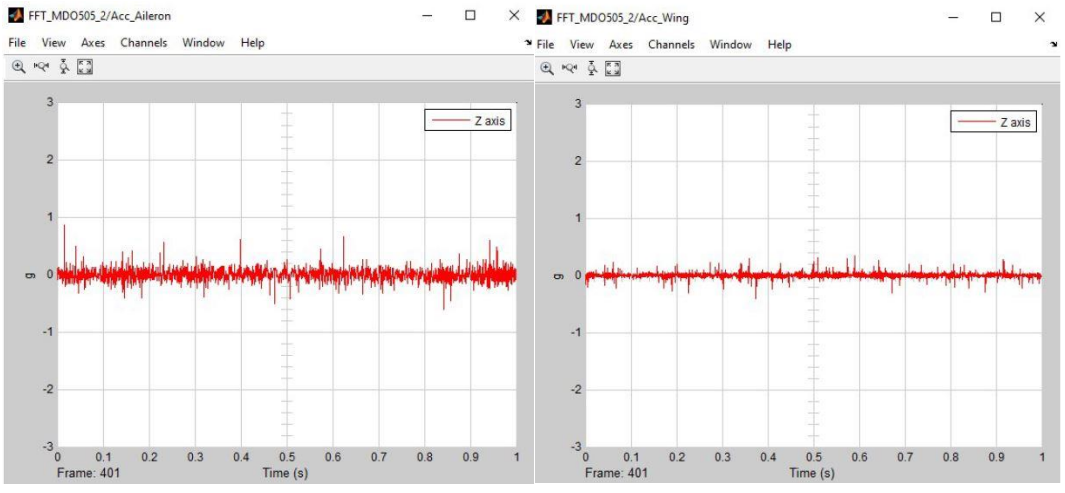

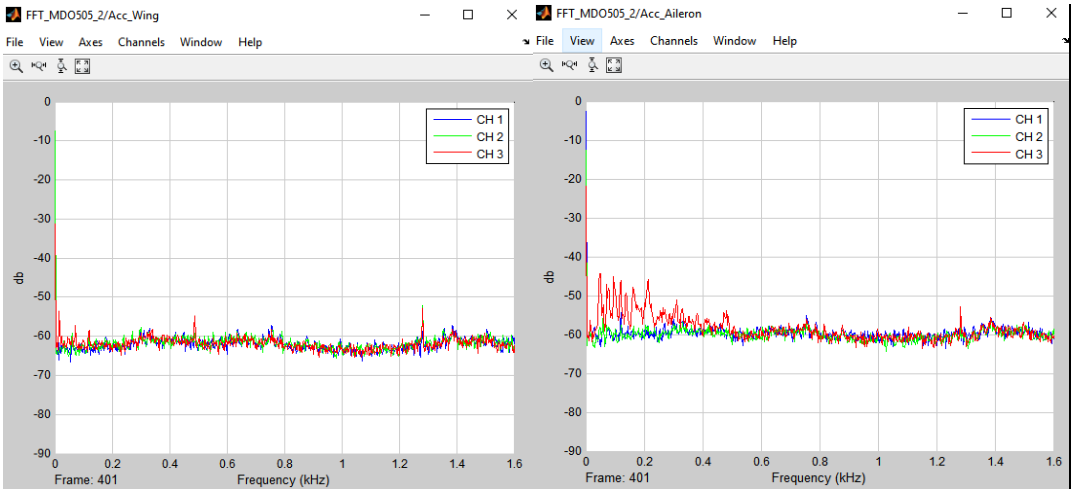

Figure 21. Case 1 - Wing with aileron deflection 2° up at Mach 0.15

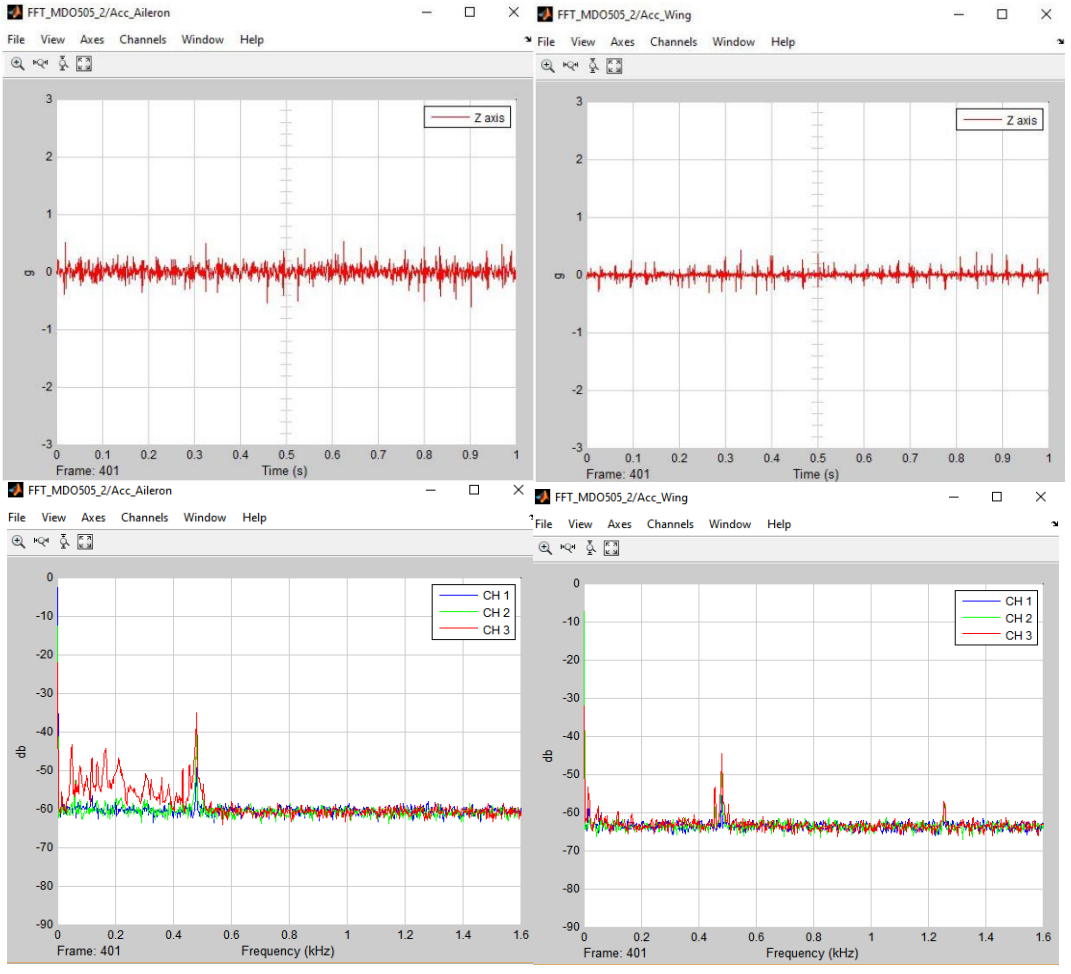

Figure 22. Case 2 - Wing with aileron deflection 4° down at Mach 0.15

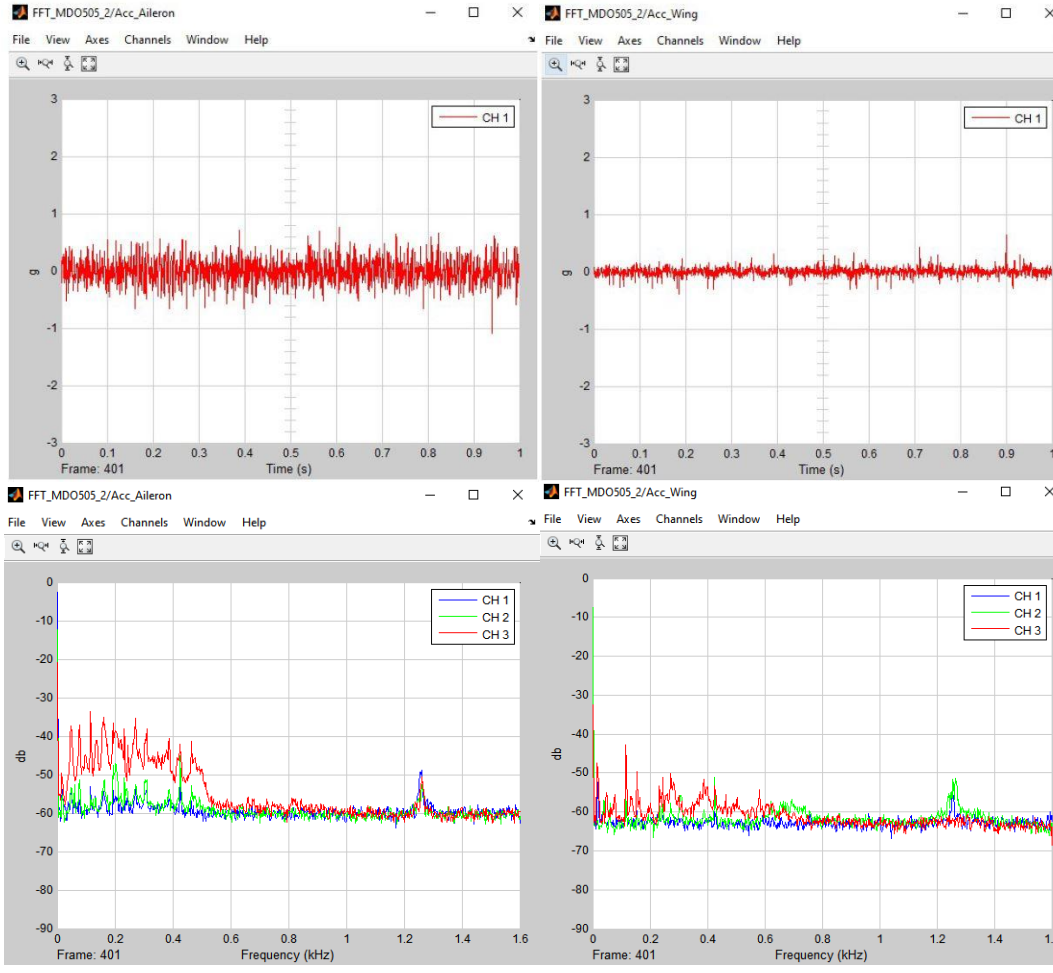

Figure 23. Case 3 - Wing with aileron deflection -4° up at Mach 0.25

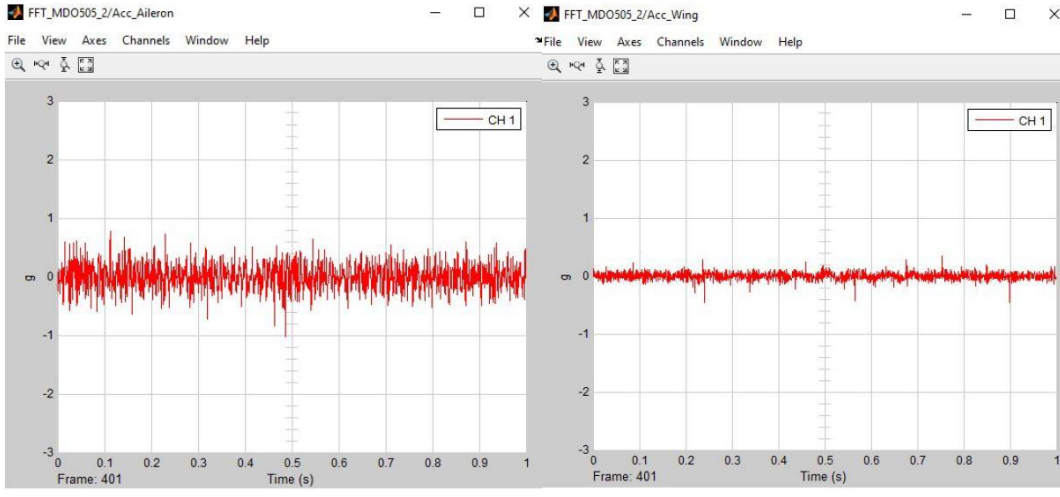

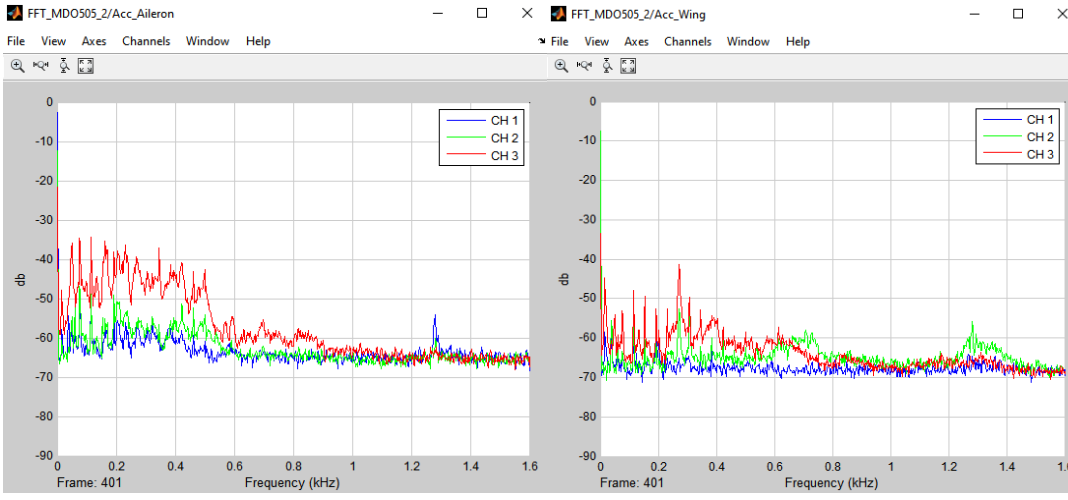

Figure 24. Case 4 - Wing with aileron deflection 5° down at Mach 0.25

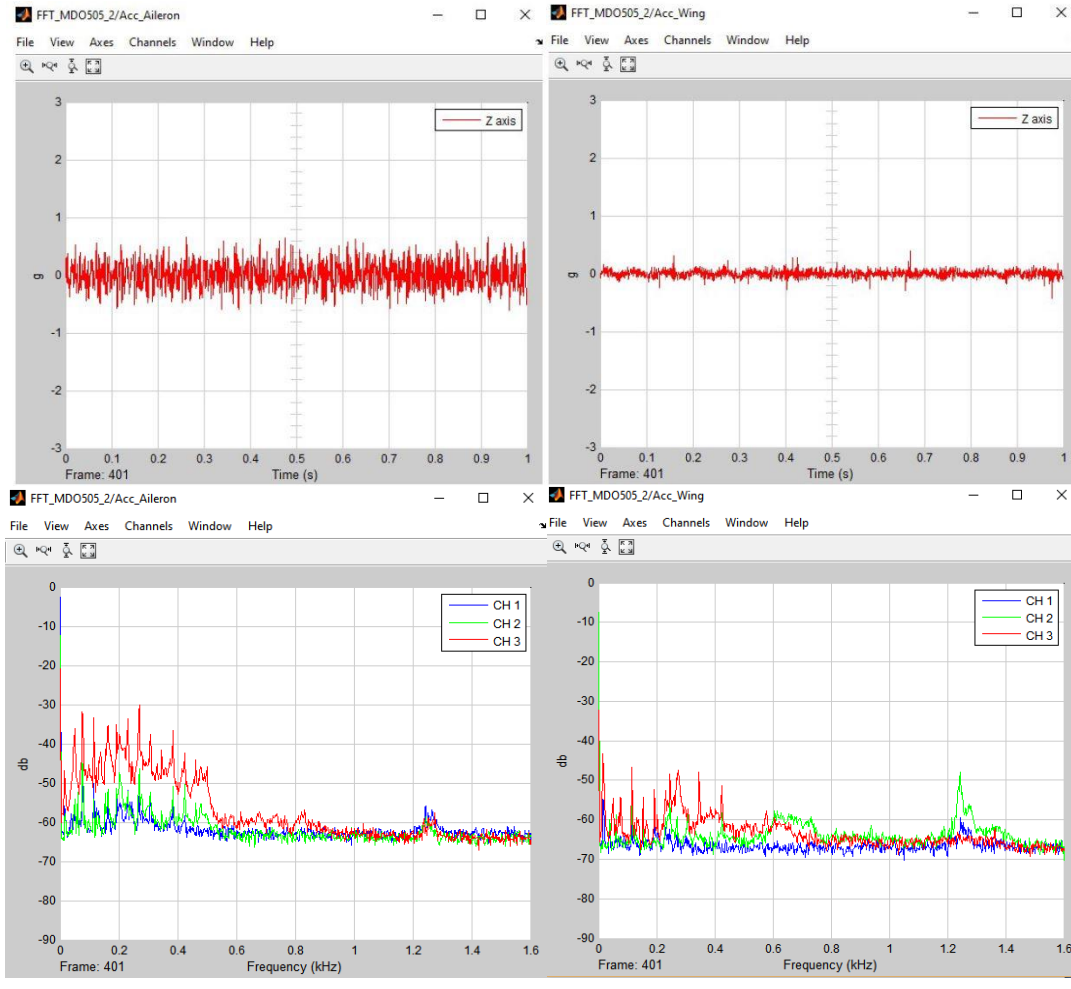

Figure 25. Case 5 - Wing with aileron deflection 1° down at Mach 0.25

From Figures 21 to 25 (a), the influence of the airspeed was observed on the accelerations; for the Mach number of 0.15 (50 m/s) the accelerations revolve around the 0.5 g for the accelerometer installed on the aileron, which is the accelerometer most sensitive to changes in amplitude due to the fact that the aileron is an almost free element (fixed by the external actuator), and therefore is the most flexible part of the wing demonstrator. The magnitude of the acceleration extracted for the Mach 0.25 (85 m/s) cases is three times the magnitude we have for Mach 0.15 (50 m/s) cases. Of course, these accelerations have small values which show small displacements as well, which confirms that the order of magnitude of the displacements predicted during the flutter analysis were correct.

In Figures 21 to 25 (b), the effect of the airspeed can also be seen, when passing from Mach number 0.15 to 0.25, but here the presence of the modes is also visible in the range 0 to 450 Hz, corresponding to first 10 modes. Channels 1, 2 and 3 represent the *x*, *y* and *z* axis. It can be observed that the axis on which the amplitude of vibrations is highest is the z axis, which is in fact oriented in the span direction of the model; it should also be noted that the amplitudes measured on the aileron are normally higher that those measured on the wing because the aileron is a flexible and movable part compared to the wing box and even to the morphing upper surface. But the magnitude of the amplitude of vibration remains less than 60dB, which for a rigid structure means that no aero-elastic effects, such as flutter, occurs at these speeds. From the wing's point of view, a mode appears at 1.3 kHz where a peak in amplitude occurs for the *y* axis, while at the same frequency the aileron has a peak in amplitude on the *x* axis (corresponding to the chord direction), but for both, the magnitude of the peak is smaller than the amplitude seen in the frequency range of 0 to 400 Hz, which means that this mode does not put in danger the structure of the wing demonstrator during tests. Overall, it can be said that by using the recorded accelerometers' data, it can be confirmed that the flutter analysis was correct in the assumption that for the speeds at which the wing demonstrator was tested, no aeroelastic dynamic or static phenomena occurred, and that the wing with aileron is a sufficiently rigid system that can safely be tested at similar or higher speeds (but remaining in the subsonic range) and no structural damages would occur.

VI. CONCLUSIONS

In the present paper, the flutter analysis and the experimental accelerometer results were discussed for a wing demonstrator with a morphing composite upper surface. The research was part of multi- disciplinary project aimed at developing a safe morphing wing technology that would improve the performances of the wing and aircraft, and that could have a fast implementation on an already existing structure. The finite element model was discussed in detail, and presented the manner in which the structure was modeled as well as the differences that occurred between the composite upper surface skin and the traditional aluminium skin. For the flutter analysis, two models were developed. The difference between the two FEM models was given by the material and properties of the upper surface between the two spar components. One model had a traditional aluminium upper surface with constant thickness, while the second model had a composite upper surface skin optimized for morphing capabilities and deformation performances, with variable thickness in both span and chord directions. The models were developed using Hypermesh software, part of the HyperWorks software package. The flutter analysis was conducted using the MSC Patran/Nastran software. For the flutter analysis the thin plate method was used to generate an aerodynamic plate with DLM boxes for the aerodynamic analysis and the coupling between structural and aerodynamic meshes was further done using thin plate

splining method. The analysis was done using the p-k method for calculating the modal displacements and frequencies. The numerical results have shown small displacements corresponding to the first 5 modes, and the damping ratio curve for each mode calculated for a range of speeds has shown that not flutter phenomena was expected to take place for the speeds that were tested in the wind tunnel. The analysis of the two models has shown that the composite skin had a minimal influence on the aero-elastic behavior of the wing; the wing with composite upper-surface optimized for morphing capabilities performed in almost the same manner as the wing with traditional aluminium skin of constant thickness. This fact has shown that during the structural optimization and sizing, and through the composite skin optimization process, the structural criteria demanded by the industry partner was respected, and the results were successful in that the wing model equipped with composite upper surface has its rigidity properties close to those of the aluminium skin, while the flexibility needed for active controlled deformation was retained. The experimental data recorded by three accelerometers installed on the aileron, wing box and balance, have confirmed that analysis was correct in its prediction that flutter phenomenon would not occur and it had also shown that the small changes in speeds, as from 50 to 85 m/s, had a visible influence on the accelerations associated with the amplitudes of vibrations. Furthermore, on the frequency graphs, it was possible to visualize the main acting modes in the range of 0 to 450 Hz and to observe a mode that taking place at 1.3 kHz that was not predicted by the numerical analysis.

In conclusion, the analysis has shown that it was possible to develop a composite morphing skin that retains the behavior of an aluminium skin for a wing without endangering the structure of the wing. Both the analysis and the experimental data from accelerometers have shown that for an actively morphing wing demonstrator tested at subsonic speeds, at various angles of attack and aileron deflections, no aero-elastic effects could be observed.

ACKNOWLEDGEMENTS

We would like to indicate our appreciation for the financial support obtained in the framework of the CRIAQ MDO-505 project and for the implication of our industrial partners Bombardier Aerospace and Thales Canada. We also wish to thank NSERC for their support.
Special thanks are dues to our collaborators and leaders in this project: Mr. Patrick Germain and Mr. Fassi Kafyeke from Bombardier Aerospace, Mr. Philippe Molaret from Thalès Canada and Mr. Eric Laurendeau from École Polytechnique.

REFERENCE

[1] J. J. Joo, B. Sanders, T. Johnson & M. I. Frecker, Optimal Actuator Location within a Morphing Wing Scissor Mechanism Configuration, In *Smart Structures and Materials* (pp. 616603-616603), International Society for Optics and Photonics, March, 2006.

[2] D. A. Neal, M. G. Good, C. O. Johnston, H. H. Robertshaw, W. H. Mason & D. J. Inman, Design and Wind-Tunnel Analysis of a Fully Adaptive Aircraft Configuration, *Proceedings of AIAA/ASME/ASCE/AHS/ASC SDM, Palm Springs, California*, 2004.

[3] J. L. Reed Jr, C. D. Hemmelgarn, B. M. Pelley & E. Havens, Adaptive Wing Structures, In *Smart structures and materials* (pp. 132-142), International Society for Optics and Photonics, May, 2005.

[4] P. Poonsong, *Design and Analysis of a Multi-Section Variable Camber Wing*, (Doctoral dissertation), 2004.

[5] H. P. Monner, H. Hanselka & E. J. Breitbach, Development and Design of Flexible Fowler Flaps for an Adaptive Wing, In *5th Annual International Symposium on Smart Structures and Materials* (pp. 60-70), International Society for Optics and Photonics, 2004.

[6] R. Pecora, S. Barbarino, L. Lecce & S. Russo, Design and Functional Test of a Morphing High-Lift Device for a Regional Aircraft, *Journal of Intelligent Material Systems and Structures*, **22**(10), 1005-1023, 2011.

[7] R. Pecora, M. Magnifico, F. Amoroso, E. Monaco, Trade-Off Flutter Analysis of a Morphing Wing Trailing Edge, Proceedings of the 6th ECCOMAS Conference on Smart Structures and Materials, SMART 2013.

[8] O. G. Sugar, A. Koreanschi & R. M. Botez, *Optimization of an Unmanned Aerial System' Wing Using a Flexible Skin Morphing Wing* (No. 2013-01-2095), SAE Technical Paper, 2013.

[9] O. G. Sugar, A. Simon, A. Koreanschi & R. M. Botez, Improving The UAS-S4 Éhecal Airfoil High Angles-Of-Attack Performance Characteristics Using a Morphing Wing Approach, *Proceedings of the Institution of Mechanical Engineers, Part G: Journal of Aerospace Engineering*, 0954410015587725, 2015.

[10] A. Y. N. Sofla, S. A. Meguid, K. T. Tan & W. K. Yeo, Shape Morphing of Aircraft Wing: Status and Challenges, *Materials & Design*, **31**(3), 1284-1292, 2010.

[11] S. Vasista, L. Tong & K. C. Wong, Realization of Morphing Wings: A Multidisciplinary Challenge, *Journal of aircraft*, **49**(1), 11-28, 2012.

[12] S. Barbarino, O. Bilgen, R. M. Ajaj, M. I. Friswell & D. J. Inman, A Review of Morphing Aircraft, *Journal of Intelligent Material Systems and Structures*, **22**(9), 823-877, 2011.

[13] C. Liauzun, Aeroelastic Response to Gust Using CFD Techniques, In *ASME 2010 3rd Joint US-European Fluids Engineering Summer Meeting collocated with 8th International Conference on Nanochannels, Microchannels, and Minichannels* (pp. 269-276), American Society of Mechanical Engineers, January, 2010.

[14] S. H. Huo, Z. Yuan, F. S. Wang & Z. F. Yue, Effects of Static Aeroelasticity on Composite Wing Characteristics under Different Flight Attitudes, *Journal of Central South University*, **20**, 312-317, 2013.

[15] R. Pecora, F. Amoroso and L. Lecce, Effectiveness of Wing Twist Morphing in Roll Control, *Journal of aircraft*, Vol. **49**, No. 6, pp. 1666-1674, 2012.

[16] R. Pecora, M. Magnifico, F. Amoroso and E. Monaco, Multi-Parametric Flutter Analysis of a Morphing Wing Trailing Edge, *Aeronautical Journal* ,Vol. **118**, No. 1207, pp. 1063-1078, 2014.

[17] C. C. Xie, Y. Liu and C. Yang, Theoretic Analysis and Experiment on Aeroelasticity of Very Flexible Wing, *Science China-Technological Sciences*, Vol. **55**, No. 9, pp. 2489-2500, 2012.

[18] J. Murua, R. Palacios & J. Peiró, Camber Effects in the Dynamic Aeroelasticity of Compliant Airfoils. *Journal of Fluids and Structures*, **26**(4), 527-543, 2010.

[19] W. Shyy, H. Aono, S. K. Chimakurthi, P. Trizila, C. K. Kang, C. E. Cesnik & H. Liu, Recent Progress in Flapping Wing Aerodynamics and Aeroelasticity, *Progress in Aerospace Sciences*, **46**(7), 284-327, 2010.

[20] R. M. Botez, P. Molaret & E. Laurendeau, Laminar Flow Control on a Research Wing Project Presentation Covering a Three Year Period, In *Canadian Aeronautics and Space Institute Annual General Meeting*, April, 2007.

[21] L. Grigorie, A. V. Popov, R. M. Botez, M. Mamou & Y. Mebarki, A Morphing Wing Used Shape Memory Alloy Actuators New Control Technique with Bi-Positional and Pi Laws Optimal Combination-Part 1: Design Phase, ICINCO 2010, In *Proceedings of the 7th International Conference on Informatics in Control, Automation and Robotics*.

[22] T. L. Grigorie, A. V. Popov, R. M. Botez, M. Mamou & Y. Mébarki, On–Off and Proportional–Integral Controller for a Morphing Wing. Part 1: Actuation Mechanism and Control Design, *Proceedings of the Institution of Mechanical Engineers, Part G: Journal of Aerospace Engineering*, 0954410011408226, 2011.

[23] D. Coutu, V. Brailovski & P. Terriault, Promising Benefits of an Active-Extrados Morphing Laminar Wing, *Journal of Aircraft*, **46**(2), 730-731, 2009.

[24] A. V. Popov, R. M. Botez & M. Labib, Transition Point Detection from the Surface Pressure Distribution for Controller Design, *Journal of Aircraft*, **45**(1), 23-28, 2008.

[25] P. D. Silisteanu & R. M. Botez, *Two-Dimensional Airfoil Design for Low Speed Airfoils*, AIAA Atmospheric Flight Mechanics conference, Invited session paper, Minneapolis, MI, Etats-unis, 13-17 août 2012.

[26] S. Courchesne, A. V. Popov & R. M. Botez, New Aeroelastic Studies for a Morphing Wing, In *Proceedings of the 48th AIAA Aerospace Sciences Meeting Including the New Horizons Forum and Aerospace Exposition* (pp. 2010-56), January 2010.

[27] S. Courchesne, A. V. Popov & R. M. Botez, New Aeroelastic Studies for a Morphing Wing, *INCAS BULLETIN*, Volume **4**, Issue 2, pp. 19-28, (online) ISSN 2247–4528, (print) ISSN 2066–8201, ISSN–L 2066–8201, DOI: 10.13111/2066-8201.2012.4.2.2, March, 2012.

[28] T. L. Grigorie, A. V. Popov, R. M. Botez, M. Mamou & Y. Mébarki, On–Off and Proportional–Integral Controller for a Morphing Wing. Part 2: Control Validation–Numerical Simulations and Experimental Tests, *Proceedings of the Institution of Mechanical Engineers, Part G: Journal of Aerospace Engineering*, **226**(2), 146-162, 2012.

[29] A. V. Popov, L. T. Grigorie, R. M. Botez, M. Mamou & Y. Mébarki, Closed-Loop Control Validation of a Morphing Wing Using Wind Tunnel Tests, *Journal of Aircraft*, **47**(4), 1309-1317, 2010.

[30] T. L. Grigorie & R. M. Botez, Adaptive Neuro-Fuzzy Inference System-Based Controllers for Smart Material Actuator Modelling, *Proceedings of the Institution of Mechanical Engineers, Part G: Journal of Aerospace Engineering*, **223**(6), 655-668, 2009.

[31] T. L. Grigorie, R. M. Botez, & A. V. Popov, Adaptive Neuro-Fuzzy Controllers for an Open-Loop Morphing Wing System, *Proceedings of the Institution of Mechanical Engineers, Part G: Journal of Aerospace Engineering*, **223**(7), 965-975, 2009.

[32] A. V. Popov, L. T. Grigorie, R. M. Botez, M. Mamou, & Y. Mébarki, Real Time Morphing Wing Optimization Validation Using Wind-Tunnel Tests. *Journal of Aircraft*, **47**(4), 1346-1355, 2010.

[33] L. Piegl and W. Tiller, *The NURBS Book*, Second Edition: Springer-Verlag, 1997.

[34] A. Koreanschi, O. Sugar, R. M. Botez, Drag Optimization of a Wing Equipped with a Morphing Upper Surface, accepted for publication in the *Royal Aeronautical Journal*, 2015.

[35] A. Korenschi, O. Sugar, R. M. Botez, Numerical and Experimental Validation of a Morphed Wing Geometry Using Price-Païdoussis Wind Tunnel Testing, accepted under revision in *The Aeronautical Journal*, 2015.

[36] A. Koreanschi, O. Ş. Gabor, T. Ayrault, R. M. Botez, M. Mamou & Y. Mebarki, Numerical Optimization and Experimental Testing of a Morphing Wing with Aileron System, In *24th AIAA/AHS Adaptive Structures Conference* (p. 1083), 2016.

[37] O. S. Gabor, A. Koreanschi & R. M. Botez, Low-Speed Aerodynamic Characteristics Improvement of ATR 42 Airfoil Using a Morphing Wing Approach, In *IECON 2012-38th Annual Conference on IEEE Industrial Electronics Society* (pp. 5451-5456), IEEE, October, 2012.

[38] F. Michaud, *Design and Optimization of a Composite Skin for an Adaptive Wing*, Master Of Science Thesis, Ecole De Technologie Superieure, Montreal, Canada, 2014.

[39] * * * http://www.altairhyperworks.com/hwhelp/Altair/hw12.0/help/hm/hmbat.aspx?hypermesh.htm, consulted in January 2016.

[40] * * * http://www.mscsoftware.com, consulted in January 2016.

[41] W. P. a. J. Rodden, H. Erwin, *MSC/NASTRAN Aeroelastic Analysis User's Guide*, V**68**, The MacNeal-Schwendler Corporation, 1994.

[42] * * * ZAERO, Version8.5, theoretical manual.

[43] C. A. Baxevanou, P. K. Chaviaropoulos, S. G. Voutsinas & N. S. Vlachos, Evaluation Study of a Navier–Stokes CFD Aeroelastic Model of Wind Turbine Airfoils in Classical Flutter, *Journal of wind engineering and industrial aerodynamics*, **96**(8), 1425-1443, 2008.

[44] L. H. van Zyl & M. S. Maserumule, Unrestrained Aeroelastic Divergence and the PK Flutter Equation. *Journal of aircraft*, **38**(3), 588-590, 2001.

[45] W. P. Rodden & E. D. Bellinger, Aerodynamic Lag Functions, Divergence, and the British Flutter Method. *Journal of Aircraft*, **19**(7), 596-598, 1982.

[46] * * * Kulite Semiconductor Products, Http://Kulite.Com/

[47]* * * Analog.Devices. URL: http://www.analog.com/en/products/mems/mems-accelerometers/adxl326.html#product-overview.